



# Enhanced 4-chlorophenol Degradation under Visible and Solar Radiation through TiO<sub>2</sub>/g-C<sub>3</sub>N<sub>4</sub> Z-Scheme Heterojunction

Karla Faquine Rodrigues <sup>1,\*</sup> , Nicolas Perciani de Moraes <sup>2</sup> , Alan Silva dos Santos <sup>1</sup> , Thaís Larissa do Amaral Montanheiro <sup>1</sup> , Tiago Moreira Bastos Campos <sup>1</sup> , Gilmar Patrocínio Thim <sup>1</sup> , Liana Alvares Rodrigues <sup>2</sup> , Deborah Dibbern Brunelli <sup>1</sup> 

<sup>1</sup> Instituto Tecnológico de Aeronáutica (ITA), São José dos Campos-SP, 12228-904, Brazil

<sup>2</sup> Escola de Engenharia de Lorena – Universidade de São Paulo (ELL-USP), Lorena-SP, 12602-810, Brazil

\* Correspondence: [kafaquine@gmail.com](mailto:kafaquine@gmail.com) (K.F.R.);

Scopus Author ID 57207201766

Received: 9.03.2022; Accepted: 13.04.2022; Published: 31.05.2022

**Abstract:** The efficient remediation of the persistent organic pollutant known as 4-chlorophenol (4CP) in aqueous effluent presents a challenge for a wide array of industries due to its elevated toxicity and resistance to natural degradation processes. This study proposes the development of a hybrid photocatalyst composed of titanium dioxide (TiO<sub>2</sub>) and graphitic carbon nitride (g-C<sub>3</sub>N<sub>4</sub>), aiming to increase the efficiency of photocatalytic degradation of 4CP under solar and visible radiation through the formation of Z-scheme heterojunction between the semiconductors. The results showed that the synthesis of the TiO<sub>2</sub>/g-C<sub>3</sub>N<sub>4</sub> binary material was successful by X-ray diffractometry and infrared spectrometry. Furthermore, the addition of g-C<sub>3</sub>N<sub>4</sub> to TiO<sub>2</sub> led to optical and morphological modifications, such as the pore volume increase and gap energy of TiO<sub>2</sub>/g-C<sub>3</sub>N<sub>4</sub>. Concerning the photocatalytic evaluation, the main results indicate that photocatalytic activity under visible radiation of the TiO<sub>2</sub>/g-C<sub>3</sub>N<sub>4</sub> improved by 44.8% compared to pure TiO<sub>2</sub>, whereas an improvement of 30.5% was obtained under simulated solar radiation. This improvement in efficiency was further corroborated by chronoamperometry tests, which demonstrated a higher photocurrent generation for the TiO<sub>2</sub>/g-C<sub>3</sub>N<sub>4</sub>. The radical generation mechanism suggested the creation of an effective Z-scheme heterojunction between the semiconductors, as the formation of both hydroxyl and superoxide radicals was observed.

**Keywords:** titanium dioxide; graphitic carbon nitride; photocatalysis; 4-chlorophenol; Z-scheme heterojunction.

© 2022 by the authors. This article is an open-access article distributed under the terms and conditions of the Creative Commons Attribution (CC BY) license (<https://creativecommons.org/licenses/by/4.0/>).

## 1. Introduction

Environmental pollution caused by the intense industrial activity to the ecosystem is a major problem of our present time. The environmental impacts caused by the release of toxic industrial effluents without proper treatment and management are considerable, englobing risks to human beings and aquatic life in rivers, lakes, and seas [1,2].

4-chlorophenol (4CP) is an organic pollutant used to manufacture plastics, textiles, leather products, pesticides, household preservatives, and pharmaceuticals [3]. 4CP is an organic compound with high toxicity and resistance to natural degradation, leading to a variety of harmful effects when not treated correctly in industrial effluents, such as infections in the respiratory system, disorders of the mucous membranes, skin irritations, burns, convulsions,

and carcinogenic effects [3,4,5]. Thus, developing efficient 4CP remediation processes is of the utmost importance [6].

Among new technologies developed for effluent treatment, the class known as advanced oxidative processes (AOPs) has attracted considerable attention in the last years [7,8]. These processes are recognized by their ability to degrade organic molecules in an aqueous medium through oxidation reactions, which are propagated by generating reactive oxygen species (ROSs) [9,10]. In the context of AOPs, heterogeneous photocatalysis presents itself as a promising method to degrade organic compounds [11].

The International Union of Pure and Applied Chemistry (IUPAC) defines photocatalysis as the “change in the rate of a chemical reaction or its initiation under the action of ultraviolet, visible or infrared radiation in the presence of a substance – the photocatalyst – that absorbs light and is involved in the chemical transformation of the reaction partners” [12]. Usually, the material used for this application is a semiconductor, which can be characterized by the presence of a valence band (VB) and a conduction band (CB) separated by an energy discontinuity called bandgap ( $E_{\text{gap}}$ ) [13]. When subjected to a radiation source of an adequate wavelength, the electrons ( $e^-$ ) present in the VB is promoted to the CB, leaving electron holes, also known as vacancies ( $h^+$ ), in the VB [14]. The  $e^-$  and the  $h^+$  are called charge carriers and, when generated, will lead to the formation of the ROSs (mainly hydroxyl and superoxide active radicals) through the reactions with adsorbed water and oxygen [15,16].

Amidst several semiconductors, titanium dioxide ( $\text{TiO}_2$ ) has been widely applied in heterogeneous photocatalysis, and it is often used to degrade drugs, dyes, biological components, and pesticide residues, among other pollutants [17,18]. This material shows great activity under ultraviolet radiation, low toxicity, good stability, and low cost. However, due to its bandgap energy (3.2 eV), this semiconductor does not display high efficiency under solar or visible light. Thus, the photocatalytic efficiency of the  $\text{TiO}_2$  must be optimized through adequate structural modifications, such as the formation of Z-scheme heterojunctions with another semiconductor of adequate electronic structure [19-21]. This type of heterojunction is responsible for separating charge carriers during photoexcitation, inhibiting the recombination process and thus elevating the quantum photocatalytic efficiency [22,23]. In this sense, graphitic carbon nitride ( $g\text{-C}_3\text{N}_4$ ) emerges as a suitable semiconductor for coupling with titanium oxide due to  $g\text{-C}_3\text{N}_4$  low bandgap energy and the matching band structures between semiconductors are adequate for the Z-scheme heterojunction.

Therefore, this study proposes the preparation of hybrid material composed of  $\text{TiO}_2$  and  $g\text{-C}_3\text{N}_4$  to enhance the photocatalytic degradation of 4CP under visible and simulated solar radiation.

## 2. Materials and Methods

### 2.1. Materials.

Metallic titanium (Ti) machining scraps were donated by the Escola de Engenharia de Lorena (EEL/USP). Hydrofluoric acid (HF) (40% w/w, Neon Analytic Reactants), nitric acid ( $\text{HNO}_3$ ) (65% w/w, Synth), ammonium hydroxide ( $\text{NH}_4\text{OH}$ ) (30% w/w, Synth), and urea (99% w/w, Synth) were used as received. 4CP (99% w/w) was purchased from Sigma Aldrich. Deionized water (DI) was used in all experiments.

## 2.2. Preparation of $\text{TiO}_2$ photocatalyst.

$\text{TiO}_2$  was prepared by dissolving Ti machining scraps in an acidic medium ( $\text{HF}/\text{HNO}_3$ ). For this, 1.2 g of Ti was added to a polypropylene beaker with 7.2 mL of DI water. Subsequently, 2.4 mL of HF was added dropwise to the beaker, followed by adding 1.2 mL of  $\text{HNO}_3$ . After complete dissolution of the Ti, the solution was filtered the resulting filtrate was placed in a beaker under magnetic stirring. Then, the  $\text{NH}_4\text{OH}$  solution (38.4 mL, 1:3 v/v) was added to cause the precipitation of the titanium hydroxide. The material was washed with DI water until neutral pH was observed in the filtrate and then placed in an oven (Splabor/SP-400) at 100 °C until a constant mass was obtained. Finally, the material was macerated, sifted through a 325 mesh sieve, and named  $\text{TiO}_2$ .

## 2.3. Preparation of g- $\text{C}_3\text{N}_4$ photocatalyst.

20 g of urea were added to an alumina crucible with a lid, which was then placed in a muffle furnace (VRC/LEXUS) and heated to 550 °C with a heating ramp of 5 °C  $\text{min}^{-1}$ , remaining for 2 h at 550 °C. The resulting material was washed with approximately five liters of DI water. The sample was then dried in an oven (Splabor/SP-400) at 80 °C until a constant mass was obtained. The dry sample was macerated, sifted through a 325 mesh sieve, and named g- $\text{C}_3\text{N}_4$ .

## 2.4. Preparation of $\text{TiO}_2/\text{g-C}_3\text{N}_4$ photocatalyst.

As described previously, 1.2 g of Ti was added to a polypropylene beaker with 7.2 mL of DI water. Subsequently, 2.4 mL of HF was added dropwise to the beaker, followed by adding 1.2 mL of  $\text{HNO}_3$ , also dropwise. After the complete dissolution of the Ti, the solution was filtered using a vacuum pump, and the filtrate was placed in a beaker under magnetic stirring. 0.18 g of g- $\text{C}_3\text{N}_4$  was added to the dissolved Ti solution and kept under magnetic stirring until it was completely dispersed. Then an  $\text{NH}_4\text{OH}$  solution (38.4 mL, 1:3 v/v) was added. The material was washed with DI water until neutral pH was observed in the filtrate and placed in an oven at 100 °C until a constant mass was obtained. Finally, the material was macerated, sifted through a 325 mesh sieve, and named  $\text{TiO}_2/\text{g-C}_3\text{N}_4$ .

## 2.5. Samples characterization.

The X-ray diffractometry (XRD) technique was used to determine the crystalline structures present in the prepared materials, for which the Empyrean X-ray diffractometer (PANalytical) was used, with a copper tube operating at 40 kV and 40 mA for  $2\theta$  values between 10 and 90 °, with  $\Delta\theta = 0.017^\circ$  and a sweep speed of 0.42 °  $\text{s}^{-1}$ . The chemical structure of the molecules present in the samples was analyzed by FT-IR spectroscopy, using a Perkin Elmer spectrometer (Frontier model) in the region from 4000 to 400  $\text{cm}^{-1}$ , with 32 scans per spectrum. Diffuse reflectance spectroscopy was conducted in a UV-Vis spectrophotometer (Shimadzu UV-2600) equipped with an integrating sphere, with an acquisition interval of 220 to 800 nm, using barium sulfate as reference material. The thermal stability of the samples was evaluated by TGA, using a PerkinElmer TGA 7 HT equipment, with a heating rate of 10 °C  $\text{min}^{-1}$ , between 30 and 700 °C, under a natural atmosphere. The micrographs of the samples were obtained by a scanning electron microscope (FESEM), TESCAN Mira 3, with a voltage of 15 kV, high vacuum, and In-Beam-SE mode. A V-Sorb 2800 equipment (Gold APP) was

used to acquire the nitrogen isotherms of the samples, which were previously thermally treated for 2 h at 120 °C (under vacuum). The nitrogen isotherms of the samples, which had previously been thermally treated for 2 h at 120 °C (under vacuum), were obtained using a V-Sorb 2800 equipment (Gold APP). The Brunauer–Emmett–Teller (BET) approach was used to calculate the 'materials' specific surface area. The total pore volume was computed at a relative pressure of 0.99, and the pore distribution was determined using the non-local density functional theory (nLDFT). An Autolab PGSTAT204 potentiostat/galvanostat was used for the chronoamperometry experiments. The following electrode system was developed within a 0.2 L quartz electrochemical cell: a saturated Ag/AgCl reference electrode, a platinum foil counter electrode, and a platinum RDE working electrode. A 0.1 mol L<sup>-1</sup> K<sub>2</sub>SO<sub>4</sub> aqueous electrolyte was employed as the experiment medium. On the platinum surface of the working electrode, materials were deposited as a microlayer. In all chronoamperometry tests, an artificial solar light source was employed (Osram Ultra Vitalux 300 W). The photocurrent generation was evaluated by applying a potential of 0.4 V (versus Ag/AgCl).

### *2.6. Photocatalytic activity measurements.*

The photocatalytic activity of the prepared samples was evaluated through the degradation of 4CP (C<sub>0</sub> = 10 mg L<sup>-1</sup>) in a jacketed batch reactor (10 cm in height and 10 cm in internal diameter). 0.1 g of the photocatalyst was added to 500 mL of 4CP solution. The temperature of 25°C was controlled by water circulation in the reactor jacket. The 4CP solutions were kept in the dark until the adsorption-desorption equilibrium was reached under magnetic stirring. After reaching adsorption-desorption equilibrium, the system was exposed to light irradiation either from a lamp simulating sunlight (OSRAM Ultra Vitalux 300 W) or a lamp emitting solely visible radiation (OSRAM Powerstar 400 W, with UV filter). In photodegradation tests, the system remained under magnetic stirring throughout the entire experiment, which was conducted for 300 min. 2 mL aliquots were collected and filtered at pre-determined intervals, and the concentration of 4CP was determined spectrophotometrically at the wavelength of 224 nm using a Shimadzu UV-2600 spectrophotometer.

The photocatalytic degradation mechanism was evaluated using the following chemical agents as scavengers: nitrogen gas at a flow rate of 0.3 L min<sup>-1</sup> (superoxide inhibitor), isopropyl alcohol (4% v/v, hydroxyl scavenger), potassium chromate (0.025 mol L<sup>-1</sup>, electron scavenger) and sodium oxalate (0.5 mol L<sup>-1</sup>, vacancy scavenger). The tests were carried out using the same methodology proposed in the previous paragraph.

## **3. Results and Discussion**

### *3.1. Characterization.*

The X-ray diffraction technique was applied to identify the crystal structures of the synthesized materials and the influence of g-C<sub>3</sub>N<sub>4</sub> addition on the crystallinity and size of TiO<sub>2</sub> crystallites. Figure 1 shows the diffractograms of TiO<sub>2</sub>, g-C<sub>3</sub>N<sub>4</sub>, and TiO<sub>2</sub>/g-C<sub>3</sub>N<sub>4</sub> samples.

The diffraction peaks of the TiO<sub>2</sub> sample are located at the following 2θ angles: 25.4 °, 37.0 °, 38.0 °, 48.1 °, 53.9 °, 55.1 °, 62.8 °, 68.9 °, 70.3 °, 75.2 °, and 82.7 °, which correspond to the respective planes: (101), (103), (004), (200), (105), (211), (204), (116), (220), (215), and (224). These planes can be attributed to the TiO<sub>2</sub> tetragonal crystalline phase known as anatase [24], according to the JCPDS file number 01-073-1764.

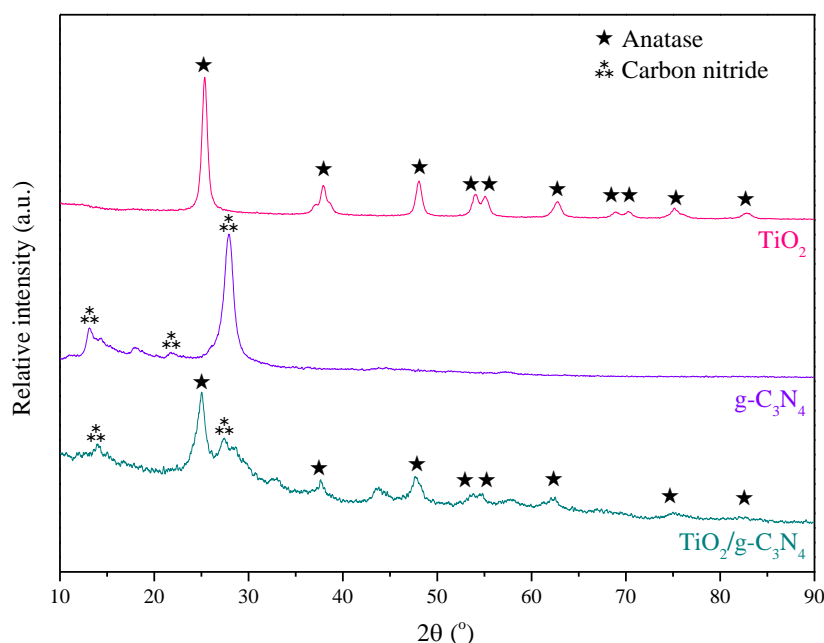


**Figure 1.** X-ray diffractograms of samples TiO<sub>2</sub>, g-C<sub>3</sub>N<sub>4</sub>, and TiO<sub>2</sub>/g-C<sub>3</sub>N<sub>4</sub>.

The diffraction peaks located at approximately 13 °, 21 °, and 27 ° in the g-C<sub>3</sub>N<sub>4</sub> sample diffractogram are associated with the (001), (100), and (002) reflection planes of the hexagonal structure of g-C<sub>3</sub>N<sub>4</sub>, respectively [25]. In the X-ray diffractogram of the TiO<sub>2</sub>/g-C<sub>3</sub>N<sub>4</sub> sample, the diffraction peaks present are associated with both TiO<sub>2</sub> and g-C<sub>3</sub>N<sub>4</sub>, confirming the presence of both semiconductors in the hybrid material.

Crystallite size is a parameter that can be determined from the data provided by the X-ray diffractograms and mathematical adjustments. According to the literature, crystallite size is directly associated with the photocatalytic properties of a material. Strauss *et al.* (2014) studied the influence of crystallite size on the photocatalytic activity of titanium dioxide and observed that the smaller the crystallite, the more efficient the photocatalyst sample [26]. Thus, it is expected that the smaller the crystallite size, the more efficient the photocatalyst will be. The crystallite size was estimated using the Scherrer relation, presented in Equation 1 [27]:

$$d = \frac{K\lambda}{\beta \cos \theta} \quad (1)$$

Where d is the crystallite size, K represents the proportionality constant (0.94), λ is the wavelength of the CuKα x-ray emission (0.154 nm), β is full width at half maximum (FWHM, in radians), and θ is the diffraction angle. To calculate the crystallite size, the FWHM of the peak located at 25.4 ° was used for the titanium dioxide.

The estimated anatase apparent crystallite sizes were 11.9 and 9.3 nm for the TiO<sub>2</sub> and TiO<sub>2</sub>/g-C<sub>3</sub>N<sub>4</sub> samples. According to these values, better efficiency in the photodegradation of 4CP is expected from TiO<sub>2</sub>/g-C<sub>3</sub>N<sub>4</sub>, as it possesses the smallest apparent crystallite size.

The FT-IR spectroscopy technique was used to characterize the chemical structure of the materials. Figure 2. shows the FT-IR spectra of TiO<sub>2</sub>, g-C<sub>3</sub>N<sub>4</sub>, and TiO<sub>2</sub>/g-C<sub>3</sub>N<sub>4</sub> samples.

The characteristic bands of the TiO<sub>2</sub> sample spectrum are located at approximately 3300, 1650, and 450 cm<sup>-1</sup>. The band at 3300 cm<sup>-1</sup> can be associated with the vibrational stretching mode of -OH, which may be related to the water adsorbed on the sample [28]. The band at 1650 cm<sup>-1</sup> is associated with the deformation of the Ti-OH bond [29,30], and the band at 450 cm<sup>-1</sup> is attributed to the stretching vibration of the Ti-O molecule [31].

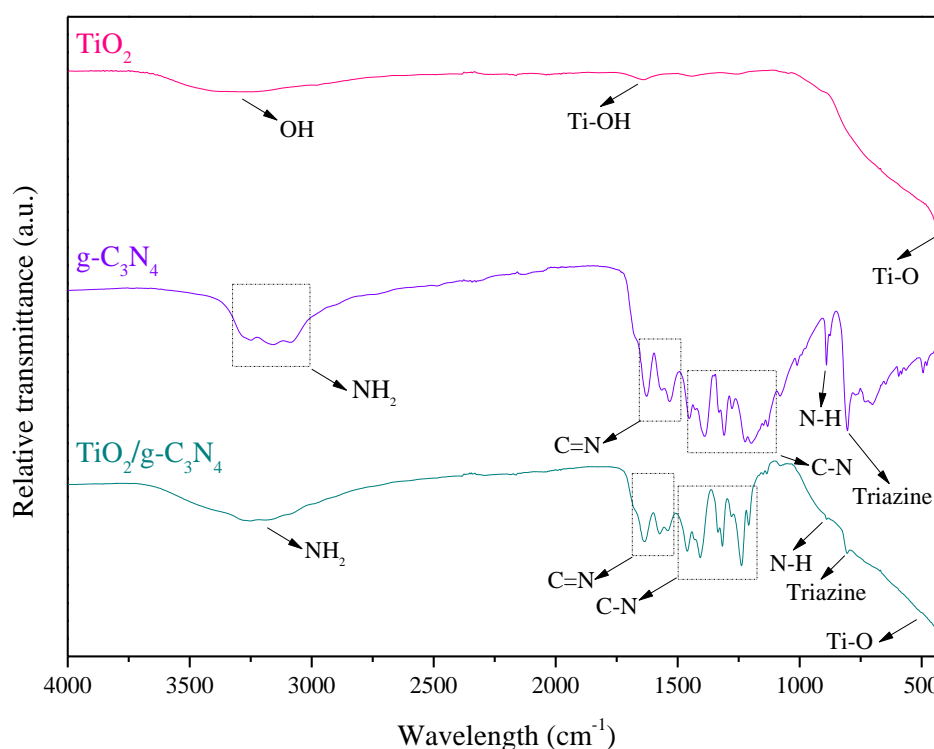


**Figure 2.** FT-IR spectra of samples  $\text{TiO}_2$ ,  $\text{g-C}_3\text{N}_4$ , and  $\text{TiO}_2/\text{g-C}_3\text{N}_4$ .

The bands present in the spectrum of the  $\text{g-C}_3\text{N}_4$  sample are characteristic of the graphitic carbon nitride structure. Firstly, the band located in the region between  $3300 - 3000 \text{ cm}^{-1}$  is related to the stretching vibration of terminal  $\text{NH}_2$  groups in the defects of the aromatic ring of the  $\text{g-C}_3\text{N}_4$  molecule [32]. The bands at  $1630$  and  $1560 \text{ cm}^{-1}$  are attributed to  $\text{C=N}$  stretch vibration, whereas the bands at  $1400$ ,  $1330$ , and  $1230 \text{ cm}^{-1}$  are associated with the  $\text{C-N}$  stretch vibration of the benzene ring of the  $\text{g-C}_3\text{N}_4$  structure [32].

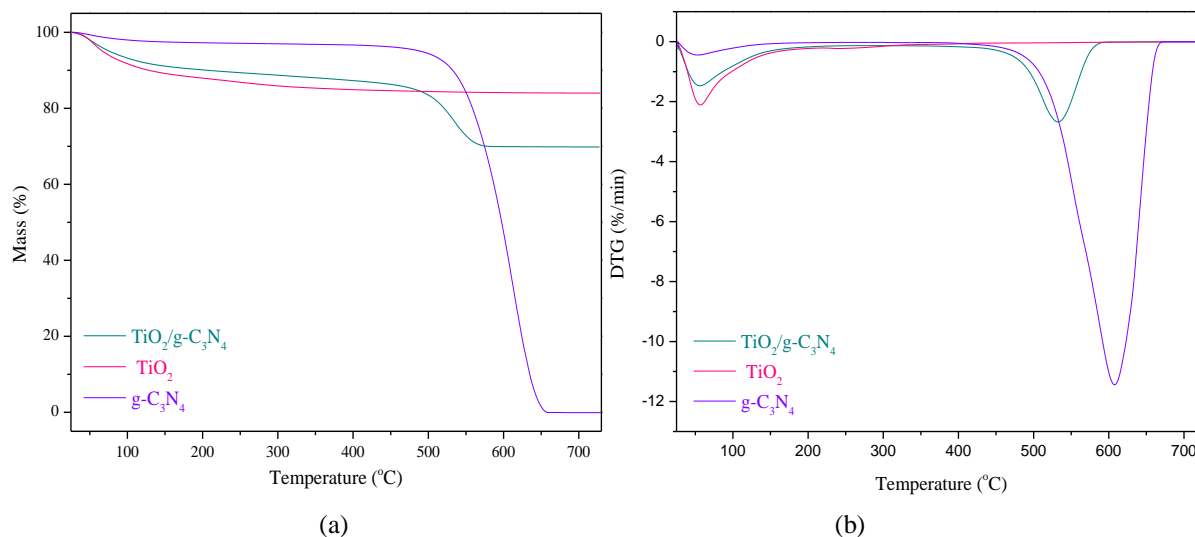


**Figure 3.** (a)TG and (b) DTG curves of samples  $\text{TiO}_2$ ,  $\text{g-C}_3\text{N}_4$ , and  $\text{TiO}_2/\text{g-C}_3\text{N}_4$ .

Finally, the band at  $889 \text{ cm}^{-1}$  is associated with the deformation mode of the  $\text{N-H}$  bond, and the band at  $805 \text{ cm}^{-1}$  can be attributed to the stretch vibration of the Tri-s-triazine ring [33]. The bands observed in the spectrum of the  $\text{TiO}_2/\text{g-C}_3\text{N}_4$  are related to a combination of the characteristic bands observed previously in the spectra of both  $\text{TiO}_2$  and  $\text{g-C}_3\text{N}_4$  samples, which further corroborates the existence of both semiconductors in the hybrid  $\text{TiO}_2/\text{g-C}_3\text{N}_4$  material.



Thermogravimetric analysis (TGA) was applied to assess the thermal stability of the synthesized samples, as well as the real content of the components of the  $\text{TiO}_2/\text{g-C}_3\text{N}_4$  sample. Figure 3 presents the thermogravimetric and derivative thermogravimetric (DTG) curves of the  $\text{TiO}_2$ ,  $\text{g-C}_3\text{N}_4$ , and  $\text{TiO}_2/\text{g-C}_3\text{N}_4$  samples.

$\text{TiO}_2$  sample curve shows a weight reduction of about 10% around 100 °C, which can also be observed in DTG, which refers to surface dehydration [34]. Afterward, the sample mass remains stable up until the end of the test, without any significant weight loss. The TG curve of the  $\text{g-C}_3\text{N}_4$  sample shows a small weight loss (~ 2%) around 100 °C, which can also be in the DTG curve, possibly associated with the removal of adsorbed water in the  $\text{g-C}_3\text{N}_4$ . Then, in the temperature range from 550 to 650 °C, an abrupt weight loss is noted and evidenced by a large peak in the DTG, which indicates the complete decomposition by combustion of  $\text{g-C}_3\text{N}_4$  [28]. The thermogravimetric curve of the  $\text{TiO}_2/\text{g-C}_3\text{N}_4$  sample exhibits two thermal degradation events. These events are indicated by two peaks in the DTG curve and by the two-fold decay of the TG curve. The first event occurs at around 100 °C and is again caused by the loss of adsorbed water, representing a 5% reduction in weight. Later, in the range of 550 to 650 °C, another event with approximately 15% weight loss is observed, associated with the decomposition by combustion of the  $\text{g-C}_3\text{N}_4$  [28]. The TG curve of the  $\text{TiO}_2/\text{g-C}_3\text{N}_4$  sample shows a remaining weight of approximately 80%, which is directly related to the actual content of  $\text{TiO}_2$  present in the material. Furthermore, it can be verified that the calcination step of the  $\text{TiO}_2/\text{g-C}_3\text{N}_4$  sample at 400 °C did not affect the  $\text{g-C}_3\text{N}_4$  fraction of the material since this component remained stable in the sample up until the temperature of 500 °C.

Diffuse reflectance spectroscopy was used to assess the light absorption and bandgap energy ( $E_{\text{gap}}$ ) of the samples produced in this study. Figure 4 shows the UV/VIS absorption spectra of  $\text{TiO}_2$ ,  $\text{g-C}_3\text{N}_4$ , and  $\text{TiO}_2/\text{g-C}_3\text{N}_4$  samples.

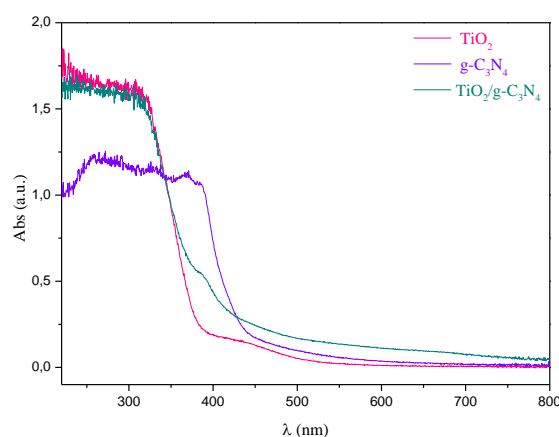


**Figure 4.** UV/VIS absorption spectra of samples  $\text{TiO}_2$ ,  $\text{g-C}_3\text{N}_4$ , and  $\text{TiO}_2/\text{g-C}_3\text{N}_4$ .

Figure 4 shows that the pure  $\text{TiO}_2$  has an absorption edge close to 380 nm, whereas the graphitic carbon nitride displays an absorption edge next to 420 nm. This result is characteristic of both materials and leads to their different bandgap energies, as the  $\text{g-C}_3\text{N}_4$  can absorb and be photoactivated by less energetic wavelengths. The hybrid  $\text{TiO}_2/\text{g-C}_3\text{N}_4$  combines the behavior exhibited by its pure components, possessing two distinct absorption edges. Furthermore, it is noticeable that the  $\text{TiO}_2/\text{g-C}_3\text{N}_4$  has a higher capacity to absorb radiation in the region between 450 – 800 nm, indicating synergy between both semiconductors toward visible light absorption.

The bandgap energy ( $E_{\text{gap}}$ ) of the samples was calculated based on the frequency of maximum absorption contained in Figure 4. Tauc relation (Equation 2) was initially used [35].

$$\alpha h\nu = B(h\nu - E_{gap})^m \quad (2)$$

where  $\alpha$  represents the absorption coefficient,  $h\nu$  is the photon energy, and  $m$  is a number that defines the type of transition, with the value of  $m = 1/2$  for direct type transitions and  $m = 2$  for indirect type.

Ghobadi *et al.* (2013) [35] described a method (Equation 3) to obtain the value of the  $E_{gap}$  based on the Tauc relation, in which only the experimental values of the radiation absorption are required.

$$\left(\frac{Abs}{\lambda}\right)^{\frac{1}{m}} = B_1 \left(\frac{1}{\lambda} - \frac{1}{\lambda_{gap}}\right) + B_2 \quad (3)$$

where  $Abs$  is the absorbance (a.u.) corresponding to a wavelength  $\lambda$ ,  $\lambda_{gap}$  is associated with the wavelength of the forbidden band ( $E_{gap}$ ),  $B_1$  and  $B_2$  are reflection constants, and  $m$ , as mentioned, is associated with the transition type. In this case,  $m = 1/2$  was considered.

Figure 5 presents the graph  $\left(\frac{Abs}{\lambda}\right)^{\frac{1}{m}}$  versus  $\frac{1}{\lambda}$  of all synthesized samples. The value of  $\frac{1}{\lambda_{gap}}$  can be defined by extrapolating the linear region of the curve  $\left(\frac{Abs}{\lambda}\right)^{\frac{1}{m}}$  to the ordinate value equal to zero<sup>35</sup>. The  $\frac{1}{\lambda_{gap}}$  values of all samples are presented in Table 1. Equation 4 [35] was used to calculate the gap energy of the synthesized materials:

$$E_{gap}(eV) = \frac{1240}{\lambda_{gap}} \quad (4)$$

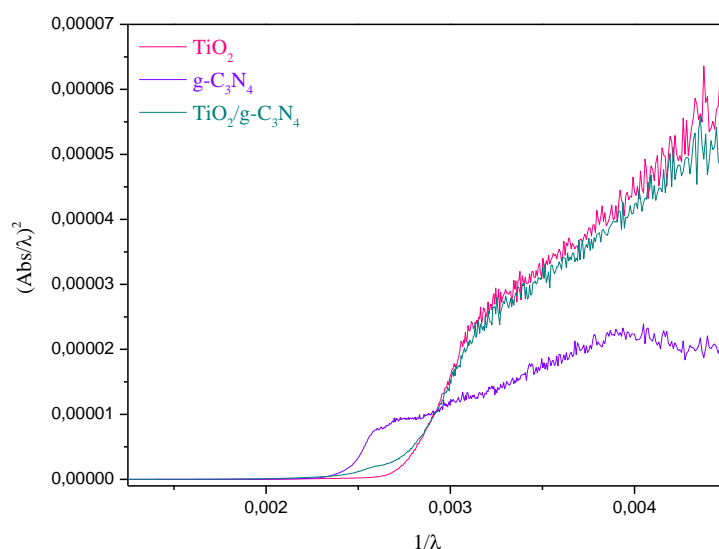


**Figure 5.**  $\left(\frac{Abs}{\lambda}\right)^{\frac{1}{m}}$  versus  $\frac{1}{\lambda}$  for the samples  $TiO_2$ ,  $g-C_3N_4$ , and  $TiO_2/g-C_3N_4$ .

**Table 1.**  $\frac{1}{\lambda}$ ,  $\lambda$  and  $E_{gap}$  values of analyzed samples.

Sample	$\frac{1}{\lambda_{gap}} \text{ (nm}^{-1}\text{)}$	$\lambda_{gap} \text{ (nm)}$	$E_{gap} \text{ (eV)}$
$TiO_2$	0,002736	365,51	3,39
$g-C_3N_4$	0,002427	412,03	3,01
$TiO_2/g-C_3N_4$	0,002661	375,79	3,29

The values presented in Table 1 indicate that the addition of  $g-C_3N_4$  to  $TiO_2$  reduces the  $E_{gap}$  for the  $TiO_2/g-C_3N_4$  sample. This  $E_{gap}$  reduction may be associated with the heterojunction coupling of  $g-C_3N_4$  to  $TiO_2$  in terms of electronic structure. Thus, it is expected that the  $TiO_2/g-$



C<sub>3</sub>N<sub>4</sub> sample will present better efficiency in the photodegradation of 4CP due to higher absorption in the visible region.

The FESEM characterization technique was used to analyze the morphology of the TiO<sub>2</sub>, g-C<sub>3</sub>N<sub>4</sub>, and TiO<sub>2</sub>/g-C<sub>3</sub>N<sub>4</sub> samples. Figure 6 shows the micrographs of the studied samples.

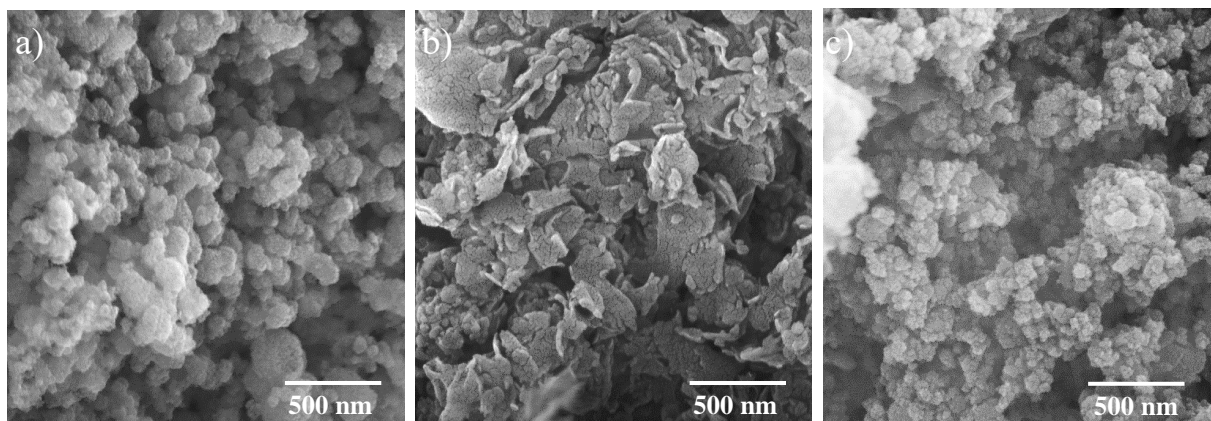


**Figure 6.** FESEM micrographs of samples: a) TiO<sub>2</sub>, b) g-C<sub>3</sub>N<sub>4</sub>, and c) TiO<sub>2</sub>/g-C<sub>3</sub>N<sub>4</sub>.

The TiO<sub>2</sub> sample comprises particles with approximately 20 nm, which exhibit a nodular morphology with a tendency to sphericity and a rough surface. The g-C<sub>3</sub>N<sub>4</sub> sample, on the other hand, is composed of sheet-like particle aggregates. The TiO<sub>2</sub>/g-C<sub>3</sub>N<sub>4</sub> sample has a morphology similar to that of the pure TiO<sub>2</sub> sample, being an agglomerate of particles with a tendency to sphericity. The appearance of the predominant TiO<sub>2</sub> in the TiO<sub>2</sub>/g-C<sub>3</sub>N<sub>4</sub> sample may be associated with the fact that the percentage of TiO<sub>2</sub> is considerably greater than the percentage of g-C<sub>3</sub>N<sub>4</sub>.

Figure 7 shows the nitrogen isotherms of the samples TiO<sub>2</sub>, g-C<sub>3</sub>N<sub>4</sub>, and TiO<sub>2</sub>/g-C<sub>3</sub>N<sub>4</sub>.

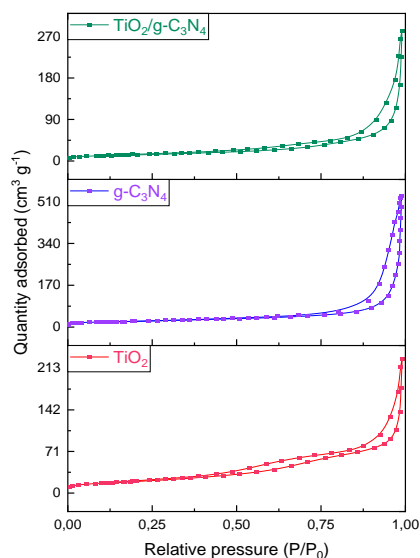


**Figure 7.** Nitrogen isotherms for the samples TiO<sub>2</sub>, g-C<sub>3</sub>N<sub>4</sub>, and TiO<sub>2</sub>/g-C<sub>3</sub>N<sub>4</sub>.

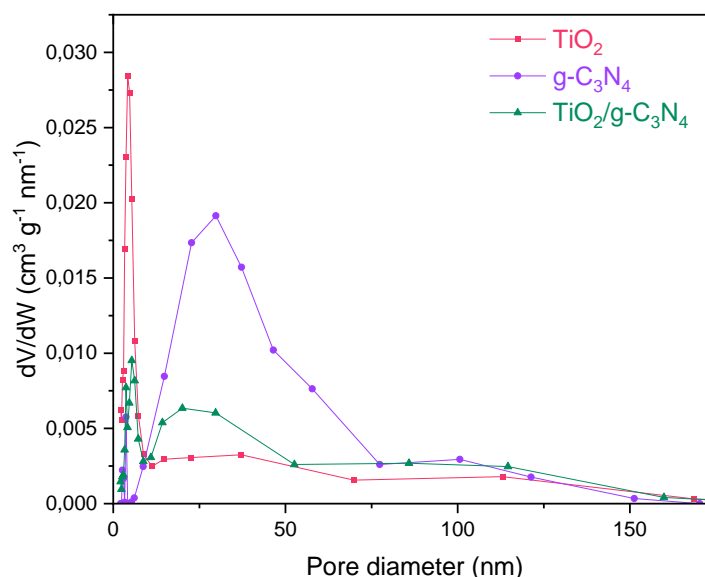
The isotherms obtained are similar to the type IV-H3 described by IUPAC and are characteristic of particle agglomerates with slit-shape pores. Values of specific surface area and pore volume were estimated using the obtained data for the materials. The results are displayed in Table 2.

**Table 2.** Specific surface area and pore volume of the samples.

Material	Specific surface area ( $\text{m}^2 \text{g}^{-1}$ )	Micropore area ( $\text{m}^2 \text{g}^{-1}$ )	Pore volume ( $\text{cm}^3 \text{g}^{-1}$ )	Micropore volume ( $\text{cm}^3 \text{g}^{-1}$ )
$\text{TiO}_2$	70.30	0	0.354	0
$\text{g-C}_3\text{N}_4$	81.43	8.77	0.833	0.0045
$\text{TiO}_2/\text{g-C}_3\text{N}_4$	46.82	1.17	0.435	0.0006

The results show that the hybrid material has a smaller surface area than its pure components. This behavior was previously reported in the literature. It has been related to the stacking of  $\text{TiO}_2$  particles on the sheet-like surface of the  $\text{g-C}_3\text{N}_4$  instead of forming large particle agglomerates, leading to a reduction in the available surface area between particles [36,37]. However, the  $\text{TiO}_2/\text{g-C}_3\text{N}_4$  displayed a larger micropore area and pore volume than the pure  $\text{TiO}_2$ , which was probably due to the properties of the  $\text{g-C}_3\text{N}_4$  in the composite.

Figure 8 shows the pore diameter distribution for the samples produced.


**Figure 8.** Pore diameter distribution for the samples  $\text{TiO}_2$ ,  $\text{g-C}_3\text{N}_4$ , and  $\text{TiO}_2/\text{g-C}_3\text{N}_4$ .

The pore diameter distribution of the  $\text{TiO}_2/\text{g-C}_3\text{N}_4$  shows a considerable reduction in the number of pores in the region between 1-10 nm compared to the pure  $\text{TiO}_2$ , which can be related to the loss in the surface area observed in Table 2. On the other hand, an increase in the number of pores ranging between 10 and 50 nm is observed, which can be linked to the increase in the pore volume observed. This increase is clearly derived from adding the  $\text{g-C}_3\text{N}_4$  to the material, as the pore distribution of the pure  $\text{g-C}_3\text{N}_4$  shows the same distribution of mesopores ranging between 10 and 50 nm.

### 3.2. Photocatalytic activity measurements.

$\text{TiO}_2$ ,  $\text{g-C}_3\text{N}_4$ , and  $\text{TiO}_2/\text{g-C}_3\text{N}_4$  samples were evaluated concerning their performance in the photodegradation of 4CP under two types of radiation: simulated sunlight and visible light. The results obtained are shown in Figures 9 and 10 for simulated sunlight and visible light, respectively.

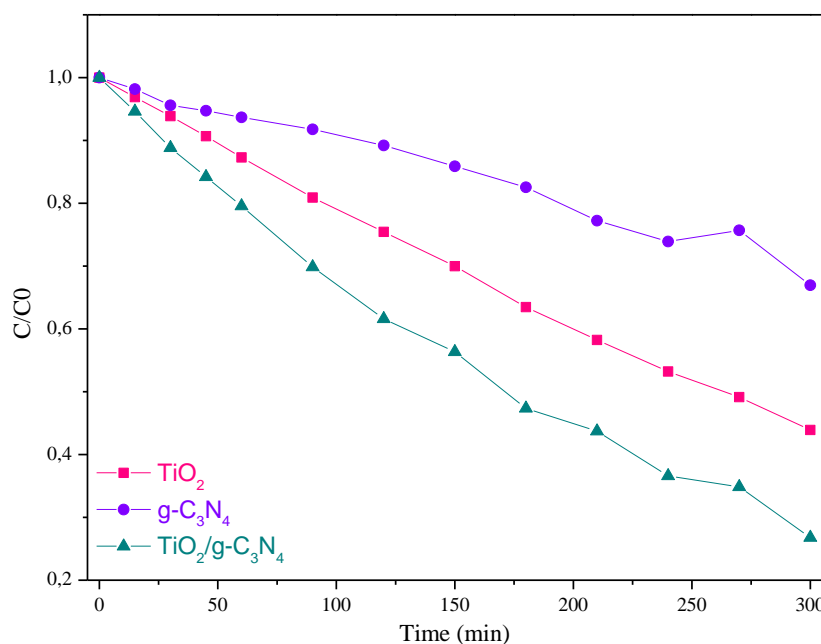


**Figure 9.** 4CP degradation curves for the samples TiO<sub>2</sub>, g-C<sub>3</sub>N<sub>4</sub>, and TiO<sub>2</sub>/g-C<sub>3</sub>N<sub>4</sub>, under simulated sunlight.

It can be seen in Figure 9 that the photocatalytic performance of the TiO<sub>2</sub>/g-C<sub>3</sub>N<sub>4</sub> sample was superior to both pure TiO<sub>2</sub> and pure g-C<sub>3</sub>N<sub>4</sub>, at 30.5% and 121.6%, respectively. This was possibly related to the increase in the absorption of less energetic radiation (Figure 4) coupled with the development of heterojunctions between the semiconductors, as the Z-scheme heterojunction promotes the separation of charge carriers, delaying the e<sup>-</sup>/h<sup>+</sup> recombination time and consequently generating a longer charge lifetime to propagate photodegradation reactions [38,39]. Thus, the results indicate that the heterojunction proposed was beneficial to the photocatalyst, leading to the production of superior material capable of degrading up to 73.2% of 4CP under simulated sunlight after 5 h.

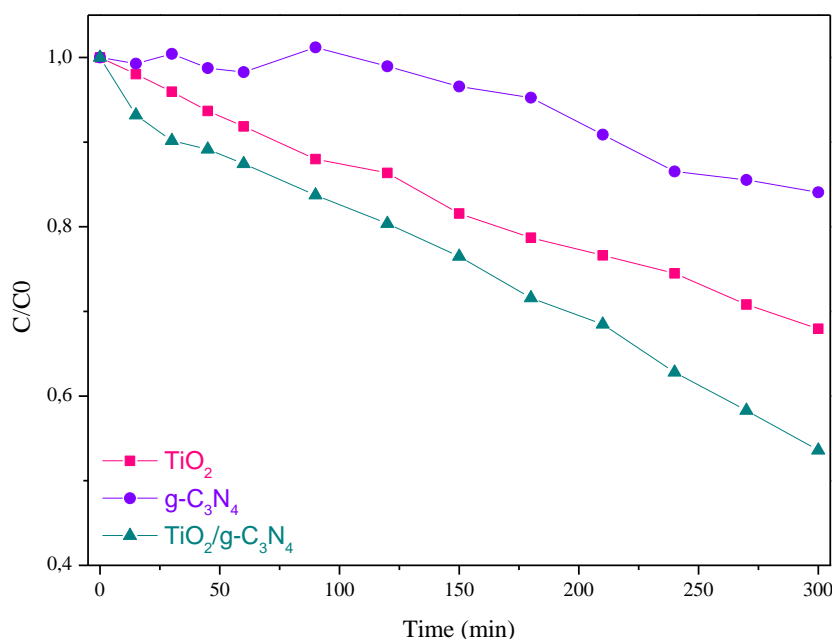


**Figure 10.** 4CP degradation curves for the samples TiO<sub>2</sub>, g-C<sub>3</sub>N<sub>4</sub>, and TiO<sub>2</sub>/g-C<sub>3</sub>N<sub>4</sub>, under visible radiation.

In agreement with the results of photodegradation under simulated sunlight, it can be seen in Figure 10 that the photocatalytic efficiency of the TiO<sub>2</sub>/g-C<sub>3</sub>N<sub>4</sub> sample was also

superior to the pure semiconductors under visible radiation. Thus, it is confirmed that bandgap reduction observed for the  $\text{TiO}_2/\text{g-C}_3\text{N}_4$  provided greater photoactivity under the visible region of the electromagnetic spectrum. The increase in efficiency of the  $\text{TiO}_2/\text{g-C}_3\text{N}_4$  sample was 44.8% compared to  $\text{TiO}_2$  and 191.4% compared to  $\text{g-C}_3\text{N}_4$ , degrading up to 46.4% of 4CP after 5 h.

To further verify the photocatalytic properties of the samples synthesized, chronoamperometry tests were performed to measure the photocurrent generation linked to each material under simulated solar radiation. The results are shown in Figure 11.

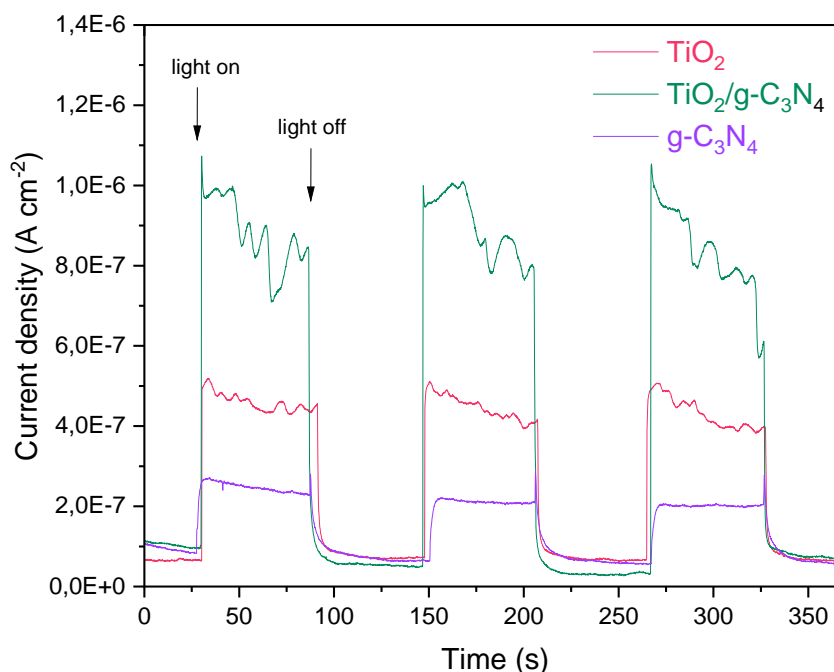


**Figure 11.** Chronoamperometry tests for the materials  $\text{TiO}_2$ ,  $\text{g-C}_3\text{N}_4$ , and  $\text{TiO}_2/\text{g-C}_3\text{N}_4$ , under simulated sunlight.

The chronoamperometry tests confirm the superiority of the  $\text{TiO}_2/\text{g-C}_3\text{N}_4$  over its components, as this material can generate a superior current density on its surface when subjected to simulated solar light [40,41]. This behavior is commonly attributed to an enhanced charged transfer capacity and photoactivity for a material, which indicates that the modification proposed was successful in the context of enhancing photocatalytic efficiency.

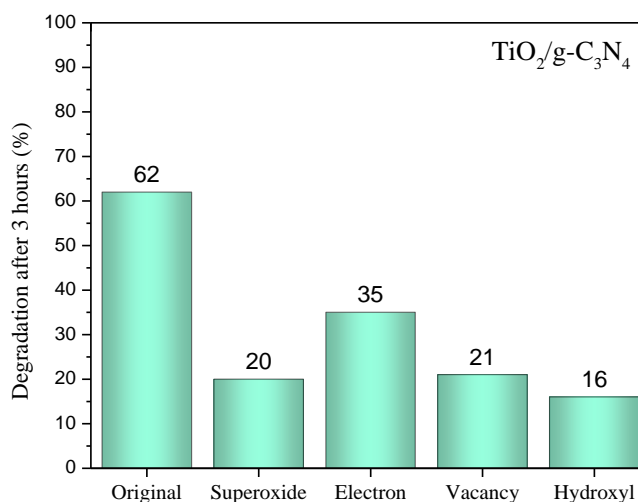


**Figure 12.** Degradation mechanism evaluation for the  $\text{TiO}_2/\text{g-C}_3\text{N}_4$ .

Photodegradation reactions are dependent on active radicals generated in the reactional system [42], which are mainly hydroxyl ( $\text{OH}^\bullet$ ) and superoxide ( $\text{O}_2^{\bullet-}$ ) radicals, as well as the charge carriers' electrons ( $e^-$ ) and vacancies ( $h^+$ ). Thus, it is important to understand the influence of these species during the photodegradation process. In this sense, the scavenger probing methodology was used to evaluate the impact of each active species on the 4CP photodegradation under simulated solar light. The scavengers were used in this study: isopropyl alcohol to inhibit hydroxyl radicals ( $\text{OH}^\bullet$ ), nitrogen gas to inhibit the superoxide radical ( $\text{O}_2^{\bullet-}$ ), potassium chromate to inhibit electrons ( $e^-$ ), and sodium oxalate to inhibit holes ( $h^+$ ) [43]. The results are shown in Figure 12.

Figure 12 shows the photodegradation results after the suppression of each species in the photodegradation process. The results show that both hydroxyl and superoxide radicals have a major role in the degradation of 4CP, as the tests with nitrogen and isopropyl alcohol led to the greatest efficiency. The suppression of electrons and vacancies also reduced photocatalytic efficiency, as these charge carriers are intrinsically involved in generating active radicals. Furthermore, the vacancies formed can directly oxidize the 4CP molecules on the material's surface, explaining the more accentuated drop observed compared to the electron scavenging. Thus, the following mechanism can be proposed for the degradation of 4CP by the  $\text{TiO}_2/\text{g-C}_3\text{N}_4$  (Equation 5-10) [44,45]:



The energy potentials of the conduction band ( $E_{CB}$ ) and valence band ( $E_{VB}$ ) for  $\text{TiO}_2$  and  $\text{g-C}_3\text{N}_4$  were determined to understand the charge separation process better. Equations 11 and 12 were applied to each semiconductor with this goal in mind. [46]:

$$E_{CB} = \chi - E^e - 0.5E_g \quad (11)$$

$$E_{VB} = E_{CB} + E_g \quad (12)$$

where  $E^e$  is the energy of free electrons vs. hydrogen ( $E^e = 4.5 \text{ eV}$ ),  $\chi$  is the electronegativity of the semiconductors ( $\chi_{\text{TiO}_2} = 5.81 \text{ eV}$  and  $\chi_{\text{g-C}_3\text{N}_4} = 4.73 \text{ eV}$ ),  $E_g$  is the gap energy,  $E_{VB}$  is the valence band potential, and  $E_{CB}$  is the conduction band potential [47,48].

For the titanium dioxide, the potential energy of the conduction and valence bands are  $-0.34 \text{ eV}$  and  $3.05 \text{ eV}$ , respectively, whereas, for the graphitic carbon nitride, the values found were  $E_{CB} = -1.27 \text{ eV}$  and  $E_{VB} = 1.73 \text{ eV}$ .

Considering the radical generation observed, the following scheme (Figure 13) is proposed to describe the heterojunction obtained in the  $\text{TiO}_2/\text{g-C}_3\text{N}_4$  hybrid.

As Figure 13 shows, the degradation of the 4CP is mainly based on the generation of hydroxyl and superoxide radicals. Considering a type-II heterojunction, the generated vacancies would be concentrated at the  $\text{g-C}_3\text{N}_4$  valence band ( $E_{VB} = 1.73 \text{ eV}$ ), which would not be able to promote the oxidation of water into hydroxyl radicals ( $E^0 = 2.73 \text{ eV}$ ) [49]. Thus, it is reasonable to assume that a Z-scheme heterojunction is present in the synthesized material,

as the formation of hydroxyl and superoxide radicals is occurring during the photodegradation of 4CP.

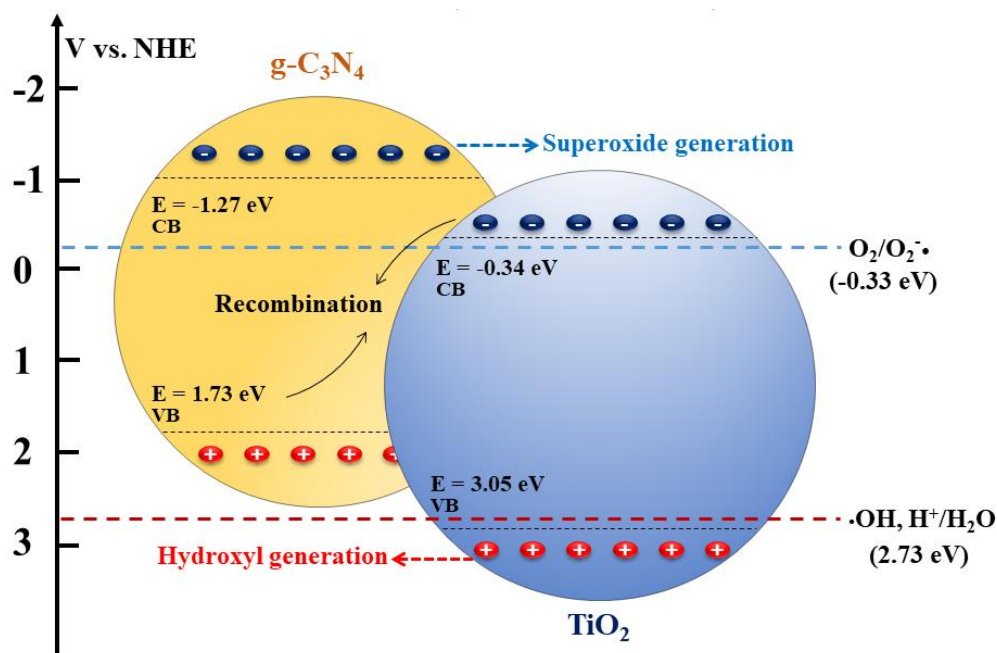


**Figure 13.** Schematic representation of the Z-scheme heterojunction between  $\text{TiO}_2$  and  $\text{g-C}_3\text{N}_4$ .

In addition to the reaction mechanism, studying the kinetics of the chemical reactions involved is also important to understanding the photocatalytic process. For this, the model proposed by Langmuir-Hinshelwood (L-H) is commonly employed to describe the kinetics of photocatalytic reactions. This model relates the degradation rate ( $r$ ) and the pollutant concentration in an aqueous medium at a given time ( $C$ ) in a mathematical equation (Equation 13) [50]:

$$r = -\frac{dC}{dt} = \frac{k_r K_{ad}}{1 + K_{ad} C} \quad (13)$$

where  $k_r$  and  $k_{ad}$  Represent the specific reaction rate and adsorption constant, respectively.

Equation 13 can be simplified according to a pseudo-first-order model (Equation 14) [50]:

$$\ln\left(\frac{C_0}{C}\right) = k_r K_{ad} t = k_{app} t \quad (14)$$

where  $C_0$  is the initial concentration of the pollutant in the photodegradation process and  $k_{app}$  is the apparent specific rate of the reaction. By plotting a graph  $\ln(C_0/C)$  versus  $t$ , it is possible to determine the  $k_{app}$  from the slope of the curve.

The pseudo-first-order model was applied to the results of the photocatalytic tests of all studied samples, both for simulated solar light and visible light. The results are shown in Table 3.

**Table 3.** Kinetic parameters obtained using the pseudo-first-order model.

Samples	$k_{app}$ ( $\text{min}^{-1}$ )	$R^2$	$k_{app}$ ( $\text{min}^{-1}$ )	$R^2$
	Simulated sunlight		Visible light	
$\text{TiO}_2$	0,0027	0,9965	0,0013	0,9969
$\text{g-C}_3\text{N}_4$	0,0012	0,9667	0,0006	0,9790
$\text{TiO}_2\text{-70/g-C}_3\text{N}_4\text{-9}$	0,0042	0,9940	0,0019	0,9837



It was verified that all prepared samples follow the pseudo-first-order kinetic reaction model, as the correlation coefficients of the linear fit ( $R^2$ ) are close to the value of 1. Regarding the specific reaction rate constant, it can be observed that the values obtained are associated with the photocatalytic performance of the materials; that is, the most efficient sample ( $\text{TiO}_2/\text{g-C}_3\text{N}_4$ ) in 4CP degradation has a higher  $k_{app}$ . This fact proves that the modification carried out to titanium dioxide was favorable to the photocatalyst efficiency.

#### 4. Conclusions

$\text{TiO}_2$ ,  $\text{g-C}_3\text{N}_4$ , and  $\text{TiO}_2/\text{g-C}_3\text{N}_4$  samples were successfully produced, as the crystal structures of  $\text{TiO}_2$  (anatase) and  $\text{g-C}_3\text{N}_4$  were characterized by X-ray diffractometry. The morphology of the  $\text{TiO}_2/\text{g-C}_3\text{N}_4$  sample was predominantly similar to  $\text{TiO}_2$ , whereas a reduced specific surface area and increased pore volume were found in the hybrid material. Diffuse reflectance spectroscopy showed an  $E_{gap}$  reduction for the  $\text{TiO}_2/\text{g-C}_3\text{N}_4$  sample compared to the pure  $\text{TiO}_2$ . The photocatalytic efficiency of the  $\text{TiO}_2/\text{g-C}_3\text{N}_4$  was significantly superior to the ones observed for the  $\text{TiO}_2$  and  $\text{g-C}_3\text{N}_4$ , under both simulated sunlight and visible light, for the photodegradation of 4CP. The chronoamperometry tests confirmed the higher photoactivity of the  $\text{TiO}_2/\text{g-C}_3\text{N}_4$  due to its enhanced photocurrent generation capacity. Furthermore, for the  $\text{TiO}_2/\text{g-C}_3\text{N}_4$ , the mechanism of radical generation was associated with the formation of both superoxide and hydroxyl radicals, suggesting the creation of an effective Z-scheme heterojunction between the semiconductors.

#### Funding

This research was funded by Coordenação de Aperfeiçoamento de Pessoal de Nível Superior – Brasil (CAPES) and Fundação de Amparo à Pesquisa do Estado de São Paulo (FAPESP), grant number 2017/24873-4; 2018/16360-0; 2018/10492-1; 2020/12507-6; 2020/12874-9.

#### Acknowledgments

The authors would like to thank the Plasma and Process Laboratory (LPP), LabMat (ITA), National Institute for Space Research (INPE), and the Instituto de Aeronautica e Espaço (IAE).

#### Conflicts of Interest

The authors declare no conflict of interest.

#### References

1. Rezende, V.M.; Lebron, Y.A.R.; Amaral, M.C.S. Enhancing industries exploitation: Integrated and hybrid membrane separation processes applied to industrial effluents beyond the treatment for disposal. *Chem. Eng. J* **2022**, *430*, <https://doi.org/10.1016/j.cej.2021.133006>.
2. Wang, Y.; Wang, Q.; Hang, Y.; Zhou, D. Decomposition of industrial pollution intensity change and reduction potential: A two-stage meta-frontier PDA method. *Sustain. Prod. Consum.* **2021**, *28*, 472–483, <https://doi.org/10.1016/j.spc.2021.06.010>.
3. Kavitha, S.; Hareendran, A.; Kurian, M. Efficient degradation of 4-chlorophenol over zirconium, nitrogen and sulphur doped cobalt nanoferrite catalysts. *Environ. Nanotechnol. Monit. Manag* **2021**, *16*, <https://doi.org/10.1016/j.enmm.2021.100540>.
4. Schmied-Tobies, M.I.H.; Murawski, A.; Schmidt, L.; Rucic, E.; Schwedler, G.; Apel, P.; Göen, T.; Kolossa-Gehring, M. Pentachlorophenol and nine other chlorophenols in urine of children and adolescents in Germany – Human biomonitoring results of the German Environmental Survey 2014–2017 (GerES V). *Environ. Research* **2021**, *196*, <https://doi.org/10.1016/j.envres.2021.110958>.

5. Sanni, S. E.; Philemon, O.; Okoro, E.E.; Oni, B.A.; Idowu, T.A.; Adegbite, O. Heterogeneous catalytic conversion of 4-chlorophenol via atomic hydrogen substitution induced by size-controlled polydisperse nanocobalt. *Chem. Eng. Sci.* **2022**, *247*, <https://doi.org/10.1016/j.ces.2021.117018>.
6. Zouzelka, R.; Kusumawati, Y.; Remzova, M.; Rathousky, J.; Pauporté, T. Photocatalytic activity of porous multiwalled carbon nanotube-TiO<sub>2</sub> composite layers for pollutant degradation. *J. Hazard. Mater.* **2016**, *317*, 52–59, <http://dx.doi.org/10.1016/j.jhazmat.2016.05.056>.
7. Khare, P.; Patel, R.K.; Sharan, S.; Shankar, R. 8 - Recent trends in advanced oxidation process for treatment of recalcitrant industrial effluents. In: *Advanced Oxidation Processes for Effluent Treatment Plants*. Shah, M.P. Ed.; Elsevier: **2021**; pp. 137-160, <http://dx.doi.org/10.1016/B978-0-12-821011-6.00008-6>.
8. Hu, H.; Miao, K.; Luo, X.; Guo, S.; Yuan, X.; Pei, F.; Qian, H.; Feng, G. Efficient Fenton-like treatment of high-concentration chlorophenol wastewater catalysed by Cu-Doped SBA-15 mesoporous silica. *J. Clean. Prod.* **2021**, *318*, <https://doi.org/10.1016/j.jclepro.2021.128632>.
9. Pham, T.H.; Bui, H.M.; Bui, T.X. Chapter 13 - Advanced oxidation processes for the removal of pesticides. In: *Current Developments in Biotechnology and Bioengineering*. Varjani, S.; Pandey, A.; Tyagi, R.D.; Ngo, H.H.; Larroche, C. Eds.; Elsevier: **2020**; pp. 309-330, <http://dx.doi.org/10.1016/b978-0-12-819594-9.00013-9>.
10. Coha, M.; Farinelli, G.; Tiraferri, A.; Minella, M.; Vione, D. Advanced oxidation processes in the removal of organic substances from produced water: Potential, configurations, and research needs. *Chemical Engineering Journal* **2021**, *414*, <https://doi.org/10.1016/j.cej.2021.128668>.
11. Hung-Lin, C.; Fu-Yu L.; Xinyu X.; Jing H.; Bo G.; Dechun Z.; Chiing-Chang, C. Visible-light-driven photocatalysis of carbon dioxide and organic pollutants by MFeO<sub>2</sub> (M = Li, Na, or K). *J. Colloid Interface Sci.* **2021**, *601*, 758–772, <https://doi.org/10.1016/j.jcis.2021.05.156>.
12. Mc Naught, A.D.; Wilkinson, A. Compendium of Chemical Terminology-Gold Book. *Iupac* 1670 **2012**, <http://old.iupac.org/publications/books/author/mcnaught.html>.
13. Guo, X.; Liu, L.; Xiao, Y.; Qi, Y.; Duan, C.; Zhang, F. Band gap engineering of metal-organic frameworks for solar fuel productions. *Coord. Chem. Rev.* **2021**, *435*, <https://doi.org/10.1016/j.ccr.2021.213785>.
14. Tokode, O.; Prabhu, R.; Lawton, L.A.; Robertson, P.K.J. Controlled periodic illumination in semiconductor photocatalysis. *J. Photochem. Photobiol. A: Chem.* **2016**, *319–320*, 96–106, <https://doi.org/10.1016/j.jphotochem.2015.12.002>.
15. Fónagy, O.; Szabó-Bárdos, E.; Horváth, O. 1,4-Benzoquinone and 1,4-hydroquinone based determination of electron and superoxide radical formed in heterogeneous photocatalytic systems. *J. Photochem. Photobiol. A: Chem.* **2021**, *407*, <https://doi.org/10.1016/j.jphotochem.2020.113057>.
16. Vikrant, K.; Weon, S.; Kim, K.H.; Sillanpää, M. Platinized titanium dioxide (Pt/TiO<sub>2</sub>) as a multi-functional catalyst for thermocatalysis, photocatalysis, and photothermal catalysis for removing air pollutants. *Appl. Mater. Today* **2021**, *23*, <https://doi.org/10.1016/j.apmt.2021.100993>.
17. Yamazaki, S.; Takaki, D.; Nishiyama, N.; Yamazaki, Y. 3 - Factors affecting photocatalytic activity of TiO<sub>2</sub>. In: *Current Developments in Photocatalysis and Photocatalytic Materials*. Wang, X.; Anpo, M.; Fu, X. Eds.; Elsevier: **2020**; pp. 23-38, <https://doi.org/10.1016/b978-0-12-819000-5.00003-5>.
18. Hasan, I.; Rana, A. A review on in SITU green synthesis of titanium dioxide nanoparticles and their photocatalytic activities. *Mater. Today: Proc.* **2021**, <https://doi.org/10.1016/j.matpr.2021.04.287>.
19. Das, S.; Mahalingam, H. Dye degradation studies using immobilized pristine and waste polystyrene-TiO<sub>2</sub>/rGO/g-C<sub>3</sub>N<sub>4</sub> nanocomposite photocatalytic film in a novel airlift reactor under solar light. *J. Environ. Chem. Eng.* **2019**, *7*, <https://doi.org/10.1016/j.jece.2019.103289>.
20. Lazau, C.; Poienar, M.; Orha, C.; Ursu, D. Development of a new “n-p” heterojunction based on TiO<sub>2</sub> and CuMnO<sub>2</sub> synergy materials. *Mater. Chem. Phys.* **2021**, *272*, <https://doi.org/10.1016/j.matchemphys.2021.124999>.
21. Liang, Y.; Li, W.; Wang, X.; Zhou, R.; Ding, H. TiO<sub>2</sub>-ZnO/Au ternary heterojunction nanocomposite: Excellent antibacterial property and visible-light photocatalytic hydrogen production efficiency. *Ceram. Int.* **2022**, *48*, 2826–2832, <https://doi.org/10.1016/j.ceramint.2021.10.072>.
22. Hassani, A.; Krishnan, S.; Scaria, J.; Eghbali, P.; Nidheesh, P.V. Z-scheme photocatalysts for visible-light-driven pollutants degradation: A review on recent advancements. *Curr. Opin. Solid State Mater. Sci.* **2021**, *25*, <https://doi.org/10.1016/j.cossms.2021.100941>.
23. Lai, Y.J.; Lee, D.J. Pollutant degradation with mediator Z-scheme heterojunction photocatalyst in water: A review. *Chemosphere* **2021**, *282*, <https://doi.org/10.1016/j.chemosphere.2021.131059>.
24. Prakash, M.; Ghosh, A.K. An investigation on optimization of instantaneous synthesis of TiO<sub>2</sub> nanoparticles and its thermal stability analysis in PP-TiO<sub>2</sub> nanocomposite. *Solid State Sci.* **2021**, *120*, <https://doi.org/10.1016/j.solidstatesciences.2021.106707>.
25. Ramezani, F.; Ghasemi-Kasman, M.; Nosratiyan, N.; Ghasemi, S.; Feizi, F. Acute administration of sulfur-doped g-C<sub>3</sub>N<sub>4</sub> induces cognitive deficits and exacerbates the levels of glial activation in mouse hippocampus. *Brain Res. Bull.* **2021**, *176*, 54–66, <https://doi.org/10.1016/j.brainresbull.2021.08.006>.
26. Strauss, M.; Pastorello, M.; Sigoli, F.A.; De Souza E Silva, J.M.; Mazali, I.O. Singular effect of crystallite size on the charge carrier generation and photocatalytic activity of nano-TiO<sub>2</sub>. *Appl. Surf. Sci.* **2014**, *319*, 151–157, <http://dx.doi.org/10.1016/j.apsusc.2014.06.071>.

27. Permana, A.D.C.; Nugroho, A.; Chung, K.Y.; Chang, W.; Kim, J. Template-free synthesis of hierarchical porous anatase TiO<sub>2</sub> microspheres with carbon coating and their electrochemical properties. *Chem. Eng. J* **2014**, *241*, 216–227, <http://dx.doi.org/10.1016/j.cej.2013.12.029>.
28. Wang, J.; Yue, M.; Han, Y.; Xu, X.; Yue, Q.; Xu, S. Highly-efficient degradation of triclosan attributed to peroxymonosulfate activation by heterogeneous catalyst g-C<sub>3</sub>N<sub>4</sub>/MnFe<sub>2</sub>O<sub>4</sub>. *Chem. Eng. J* **2020**, *391*, 123554, <https://doi.org/10.1016/j.cej.2019.123554>.
29. Escobedo-Morales, A.; Ruiz-López, I.I.; deL.Ruiz-Peralta, M.; Tepech-Carrillo, L.; Sánchez-Cantú, M.; Moreno-Orea, J.E. Automated method for the determination of the band gap energy of pure and mixed powder samples using diffuse reflectance spectroscopy. *Heliyon* **2019**, *5*, 1–19, <https://doi.org/10.1016/j.heliyon.2019.e01505>.
30. Chougala, L.S.; Yatnatti, M.S.; Linganagoudar, R.K.; Kamble, R.R.; Kadadevarmath, J.S. A simple approach on synthesis of TiO<sub>2</sub> nanoparticles and its application in dye sensitized solar cells. *J. Nano-Electron. Phys.* **2017**, *9*, [https://doi.org/10.21272/jnep.9\(4\).04005](https://doi.org/10.21272/jnep.9(4).04005).
31. Chaudhary, D.; Vankar, V.D.; Khare, N. Noble metal-free g-C<sub>3</sub>N<sub>4</sub>/TiO<sub>2</sub>/CNT ternary nanocomposite with enhanced photocatalytic performance under visible-light irradiation via multi-step charge transfer process. *J. Sol. Energy* **2017**, *158*, 132–139, <http://dx.doi.org/10.1016/j.solener.2017.09.012>.
32. Ayodhya, D.; Veerabhadram, G. Influence of g-C<sub>3</sub>N<sub>4</sub> and g-C<sub>3</sub>N<sub>4</sub> nanosheets supported CuS coupled system with effect of pH on the catalytic activity of 4-NP reduction using NaBH<sub>4</sub>. *Flat. Chem.* **2019**, *14*, <https://doi.org/10.1016/j.flatc.2019.100088>.
33. Zhu, B.; Xia, P.; Li, Y.; Ho, W.; Yu, J. Fabrication and photocatalytic activity enhanced mechanism of direct Z-scheme g-C<sub>3</sub>N<sub>4</sub>/Ag<sub>2</sub>WO<sub>4</sub> photocatalyst. *Appl. Surf. Sci.* **2017**, *391*, 175–183, <http://dx.doi.org/10.1016/j.apsusc.2016.07.104>.
34. Tekin, D.; Birhan, D.; Kiziltas, H. Thermal, photocatalytic, and antibacterial properties of calcinated nano-TiO<sub>2</sub>/polymer composites. *Mater. Chem. Phys.* **2020**, *251*, <https://doi.org/10.1016/j.matchemphys.2020.123067>.
35. Ghobadi, N. Band gap determination using absorption spectrum fitting procedure. *Int. Nano Lett.* **2013**, *3*, 2–5, <https://doi.org/10.1186/2228-5326-3-2>.
36. Alcudia-Ramos, M.A.; Fuentes-Torres, M.O.; Ortiz-Chi, F.; Espinosa-González, C.G.; Hernández-Como, N.; García-Zaleta, D.S.; Kesarla, M.K.; Torres-Torres, J.G.; Collins-Martínez, V.; Godavarthi, S. Fabrication of g-C<sub>3</sub>N<sub>4</sub>/TiO<sub>2</sub> heterojunction composite for enhanced photocatalytic hydrogen production. *Ceram. Int.* **2020**, *46*, 38–45, <https://doi.org/10.1016/j.ceramint.2019.08.228>.
37. Wu, L.C.; Zhao, H.; Jin, L.G.; Xu, H.Y. TiO<sub>2</sub>/g-C<sub>3</sub>N<sub>4</sub> heterojunctions: In situ fabrication mechanism and enhanced photocatalytic activity. *Front. Mater. Sci.* **2016**, *10*, 310–319, <https://doi.org/10.1007/s11706-016-0351-y>.
38. Shayegan, Z.; Haghighat, F.; Lee, C.S. Carbon-doped TiO<sub>2</sub> film to enhance visible and UV light photocatalytic degradation of indoor environment volatile organic compounds. *J. Environ. Chem. Eng.* **2020**, *8*, <https://doi.org/10.1016/j.jece.2020.104162>.
39. de Moraes, N.P.; da Silva, M.L.C.P.; Campos, T.M.B.; Thim, G.P.; Rodrigues, L.A. Novel synthetic route for low-cost carbon-modified TiO<sub>2</sub> with enhanced visible light photocatalytic activity: carbon content and calcination effects. *J. Sol-Gel Sci. Technol.* **2018**, *87*, 380–390, <http://dx.doi.org/10.1007/s10971-018-4700-4>.
40. She, P.; Yin, S.; He, Q.; Zhang, X.; Xu, K.; Shang, Y.; Men, X.; Zeng, S.; Sun, H.; Liu, Z. A self-standing macroporous Au/ZnO/reduced graphene oxide foam for recyclable photocatalysis and photocurrent generation. *Electrochim. Acta* **2017**, *246*, 35–42, <http://dx.doi.org/10.1016/j.electacta.2017.06.027>.
41. Lee, J.; Li, Z.; Zhu, L.; Xie, S.; Cui, X. Ti<sup>3+</sup> self-doped TiO<sub>2</sub> via facile catalytic reduction over Al(acac)<sub>3</sub> with enhanced photoelectrochemical and photocatalytic activities. *Appl. Catal. B* **2018**, *224*, 715–724, <http://dx.doi.org/10.1016/j.apcatb.2017.10.057>.
42. Tao, C.; Jia, Q.; Han, B.; Ma, Z. Tunable selectivity of radical generation over TiO<sub>2</sub> for photocatalysis. *Chem. Eng. Sci.* **2020**, *214*, <https://doi.org/10.1016/j.ces.2019.115438>.
43. Lin, C.C.; Tsai, C.W. Degradation of isopropyl alcohol using UV and persulfate in a large reactor. *Sep. Purif. Technol.* **2019**, *209*, 88–93, <https://doi.org/10.1016/j.seppur.2018.06.068>.
44. Zhang, J.; Nosaka, Y. Mechanism of the OH radical generation in photocatalysis with TiO<sub>2</sub> of different crystalline types. *J. Phys. Chem* **2014**, *118*, 10824–10832, <https://doi.org/10.1021/jp501214m>.
45. Nosaka, Y.; Nosaka, A.Y. Generation and Detection of Reactive Oxygen Species in Photocatalysis. *Chem. Rev.* **2017**, *117*, 11302–11336, <https://doi.org/10.1021/acs.chemrev.7b00161>.
46. Mousavi, M.; Habibi-Yangjeh, A.; Abitorabi, M. Fabrication of novel magnetically separable nanocomposites using graphitic carbon nitride, silver phosphate and silver chloride and their applications in photocatalytic removal of different pollutants using visible-light irradiation. *J. Colloid Interface Sci.* **2016**, *480*, 218–231, <http://dx.doi.org/10.1016/j.jcis.2016.07.021>.
47. Yan, J.; Wu, G.; Guan, N.; Li, L. Nb<sub>2</sub>O<sub>5</sub>/TiO<sub>2</sub> heterojunctions: Synthesis strategy and photocatalytic activity. *Appl. Catal. B* **2014**, *152–153*, 280–288, <http://dx.doi.org/10.1016/j.apcatb.2014.01.049>.

48. Shanmugam, V.; Muppudathi, A.L.; Jayavel, S.; Jeyaperumal, K.S. Construction of high efficient g-C<sub>3</sub>N<sub>4</sub> nanosheets combined with Bi<sub>2</sub>MoO<sub>6</sub>-Ag photocatalysts for visible-light-driven photocatalytic activity and inactivation of bacterias. *Arab. J. Chem.* **2020**, *13*, 2439–2455, <https://doi.org/10.1016/j.arabjc.2018.05.009>.
49. Kwon, B.G.; Yoon, J. Superoxide anion radical: Principle and application. *Journal of the Korean Industrial and Engineering Chemistry* **2009**, *20*, 593–602.
50. de Moraes, N.P.; Becani, R.; Silva, M.L.C.P.; Campos, T.M.B.; Thim, G.P.; Rodrigues, L.A. Effect of Nb/C ratio in the morphological, structural, optical and photocatalytic properties of novel and inexpensive Nb<sub>2</sub>O<sub>5</sub>/carbon xerogel composites. *Ceram. Int.* **2018**, *44*, 6645–6652, <http://dx.doi.org/10.1016/j.ceramint.2018.01.073>.